## 3.1 Material Selection:

The entire grinding experiments were performed on unhardened and hardened (carburized) low carbon steel. The unhardened low carbon steel bears good magnetic property whereas magnetization of hardened low carbon steel is difficult. Further, low carbon steel is widely used in automobile industry whereas hardened low carbon steel find its application in gear manufacturing industry. Thereby, the selection of such material covers a wide spectrum of application in context to grinding. Additionally, the different magnetic property of the chosen material prove the worthiness of non-destructive magnetic Barkhausen noise technique in the performance evolution of ground surface. The chemical composition of IS- 2062 low carbon steel is presented in Table 3.1.

Table 3.1: Chemical composition of IS- 2062 steel

| **Chemical elements** | **C** | **Si** | **Mn** | **P** | **S** | **Cr** | **Fe** |
|---|---|---|---|---|---|---|---|
| **%** | 0.17 | 0.045 | 0.32 | 0.007 | 0.0130 | 0.3 | Rest |

## 3.2 Hardening/Carburizing of low carbon steel:

The low carbon steel were hardened using pack carburizing process. The rectangular sample of dimension 100 $mm^{Length}$ x 50 $mm^{Width}$ x 100 $mm^{Thickness}$ were kept in a designed steel box. The samples in the box were surrounded by a mixture of (85%Charcoal + 15% $BaCO_3$)**.** The dimension of the box were chosen in such a way so as to provide an equal concentration of carbonaceous mixture around the sample. Thereafter, the steel box along with the samples were heated to a temperature of 920°C

using muffle furnace. The system were held at that particular temperature for a period of 3 hour for homogenization purpose, followed by water quenching.

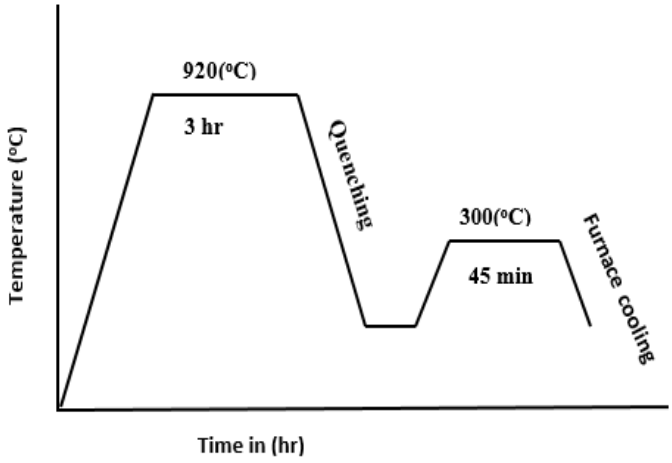


Fig.3.1 Heat treatment cycle for pack carburizing process

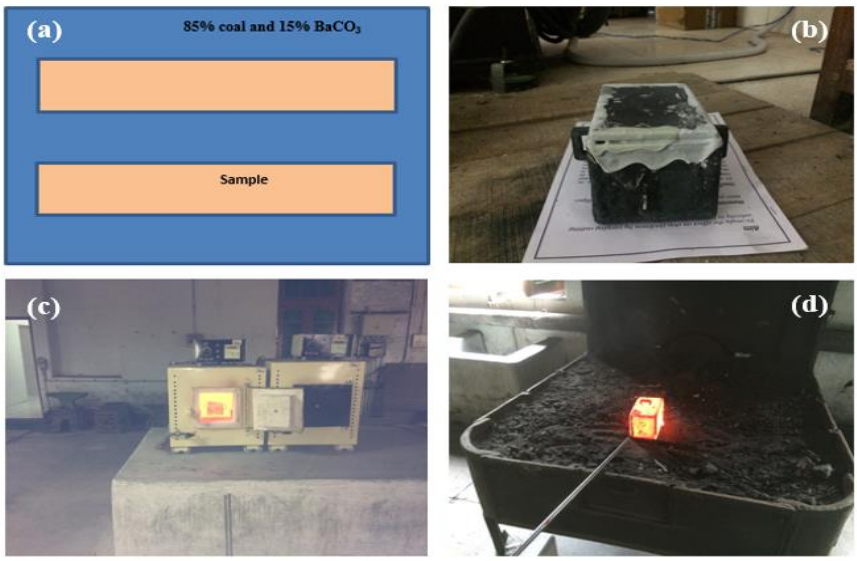


Fig.3.2 shows the steps followed during carburizing/hardening process (a) arrangement of sample inside box (b) sealing/packing of box using fire clay and sodium silicate (c) steel box inside muffle furnace (d) steel box in heated condition

Finally, the samples were tempered, by heating it to a temperature of 300°C for a period of 45 minute followed by furnace cooling. The heat treatment cycles were reported in Fig.3.1. The various steps involved during the heat treatment were reported in Fig.3.2.

### 3.3 Experimentation detail:

In present investigation, grinding test were conducted on unhardened and hardened/Carburized low carbon steel using H455 HMT (Hindustan Machine Tool Ltd., India) surface grinding machine (refer Fig.3.3). A conventional white aluminum oxide wheel were chosen for the purpose. The geometrical specification of the white aluminum oxide wheel (AA54K5V6) was 250 × 76.2 × 20 mm. The entire grinding test were conducted in plunge mode condition for 10 passes with thrice replication. The dressing of the grinding wheel was performed at a regular interval (after every four experiment) using a single point non-rotating diamond (one carat) dresser to ensure the continuity in wheel topography. Dressing overlap ratio is not considered in the present investigation as dressing under similar condition were performed throughout the experiment.

Table 3.2: Experimental condition and process parameter

| | |
|---|---|
| **Grinding machine** | H455 HMT |
| **Grinding mode** | Plunge grinding |
| **Grinding wheel** | AA54K5V6 |
| **Grinding condition** | Dry and wet |
| **Flood cooling** | Cimtech-D14 |
| **Wheel speed ($V_s$)** | 39.42 m/s |
| **Work velocity ($V_w$)** | 8,12m/min |
| **Downfeed** | 6, 12, 18, 24 μm |
| **Dressing depth** | 40 μm in 10 passes |
| **Dressing speed** | 200 mm/min |

Fig.3.3 H455 HMT (Hindustan Machine Tool Ltd., India) surface grinding machine

The test were performed by varying the grinding parameter such as downfeed (6µm, 12 µm, 18 µm and 24µm), work velocity (8m/min and 12m/min) and grinding environment (dry and wet). In order to perform grinding in wet condition, conventional cutting fluid (Cimtech-D14) is chosen which is synthetic, chlorine free and water-soluble.$L_{16}$ orthogonal array with two levels of work velocity and grinding environment and four levels of downfeed were selected in order to perform the experiment. The details of experimental condition were listed in Table 3.2 and levels of independent variable is listed in Table 3.3.

Table 3.3: Trial runs according to $L_{16}$ orthogonal array

| Trial No. | Factors and their levels | | |
|---|---|---|---|
| | Grinding Environment | Work velocity (m/min) | Downfeed (μm) |
| **1** | dry | 8 | 6 |
| **2** | dry | 8 | 12 |
| **3** | dry | 8 | 18 |
| **4** | dry | 8 | 24 |
| **5** | dry | 12 | 6 |
| **6** | dry | 12 | 12 |
| **7** | dry | 12 | 18 |
| **8** | dry | 12 | 24 |
| **9** | wet | 8 | 6 |
| **10** | wet | 8 | 12 |
| **11** | wet | 8 | 18 |
| **12** | wet | 8 | 24 |
| **13** | wet | 12 | 6 |
| **14** | wet | 12 | 12 |
| **15** | wet | 12 | 18 |
| **16** | wet | 12 | 24 |

## 3.4 Assessment of grinding performance:

The upcoming subsection reports the method of measurement of grinding forces, grinding force ratio, specific grinding energy and grinding temperature.

### 3.4.1 Measurement of grinding forces:

Forces generated during grinding operation contribute significantly to the finished product. They play a major role in determining the surface finish, part dimensions of the ground workpiece, and cycle times of the grinding operation. Interaction between wheel and the workpiece during grinding results into generation of normal grinding force, tangential grinding force and a component force in the direction of longitudinal feed. The normal grinding force effects the surface deformation and roughness of the ground workpiece, while the tangential grinding force mainly decides the power consumption and service life of the grinding wheel. However, force acting in the longitudinal feed direction has no significance in the grinding operation and are not measured usually. Grinding forces (tangential ($F_T$) and normal ($F_N$)) were measured with the help of 3-component grinding force dynamometer (IEICOS, model-610C).

### 3.4.2 Estimation of specific grinding energy:

Specific grinding energy is a basic parameter derived from the power and machining conditions, and is characterized by energy spent in removing unit volume of material. It is measure of process efficiency and indicates the difficulty of machining a workpiece material. A low specific energy process is rather considered as a more environmental friendly technique. However, specific energy consumed during grinding is nearly two fold as compared to those of metal cutting operation. This is due to, very small size grinding chips creating extremely high dislocation densities in the shear zone and also due to energy spent in undesirable rubbing and ploughing mechanism. Specific energy in grinding is estimated by eqn (3.1)

$$E_e = \frac{F_T (v_s \pm v_w)}{V_w a b} \quad (3.1)$$

Where, $F_T$ - tangential grinding force, $a$ - downfeed, b - wheel width, $v_w$ – work velocity and $v_s$ -wheel speed.

### 3.4.3 Analysis of grinding temperature:

The high temperature in grinding is the consequence of high specific grinding energy, as major proportion of this is converted into heat and get concentrated into grinding zone. This high temperature results into various types of thermal damage in the form of thermal softening, phase transformation, reduced fatigue strength, cracks and undesirable tensile residual stresses.

The total grinding energy involved during the process is the combination of energy expended in the rubbing, ploughing and cheap formation (shearing). Further, the generated grinding energy gets distributed proportionally between the workpiece, grinding fluid, chip and the grinding wheel.

The total grinding energy can be expresses in terms of total heat flux ($q_t$)

$$q_t = \frac{F_T * v_s}{L_c * b} \quad (3.2)$$

Where, $F_T$ - tangential grinding force, $v_s$ – grinding wheel velocity, b – width of cut, $L_c$ – contact length.

Length of contact ($L_c$) is a function of downfeed and wheel diameter and can be expressed in the form of eqn (3.3).

$$L_c = \sqrt{a * d_g} \quad (3.3)$$

Where, $a$ – downfeed and $d_g$- diameter of grinding wheel.

The total heat flux ($q_t$) can be expressed as follows

$$q_t = q_w + q_s + q_{ch} + q_f \qquad \text{(Rowe, 2001)} \quad (3.4)$$

Where, $q_w$- heat flux entering the work piece, $q_s$- flux entering the grinding wheel, $q_{ch}$- heat flux carried away by the chip and $q_f$- flux carried away by the grinding fluid

Heat flux carried away by the chip($q_{ch}$) can be estimated if it is assumed that chip just reach the melting temperature (Rowe, 2001) and can be expressed as follows

$$q_{ch} = \frac{\rho_w * c_w * T_{mp} * \mathrm{V_w} * a}{L_c} \qquad (3.5)$$

Where, $\rho_w$ - density of workpiece material

$c_w$ - specific heat of workpiece material

$T_{mp}$ - melting point of workpiece material

$\mathrm{V_w}$ - work velocity

The distribution of energy between workpiece and grinding wheel is discussed by Hahn (1962) and can be represented as

$$R_{ws} = \frac{q_w}{q_w + q_s} \qquad (3.6)$$

Where, $R_{ws}$ – proportion coefficient of grinding energy between workpiece and grinding wheel

Moreover, the eqn (3.6) can be further expressed in terms of grinding parameter and thermal properties of grit material and can be given as

$$R_{ws} = \frac{1}{1 + \frac{0.97 * k_g}{\beta_w \sqrt{r_0 * \mathrm{V_s}}}} \qquad \text{Hahn (1962)} \qquad (3.7)$$

Where, $\beta_w$ - thermal property of workpiece material, $r_0$ – effective radius of contact of abrasive grain, $k_g$ – thermal conductivity of abrasive grain

The thermal property of workpiece material can be rewritten as below

$$\beta_w = \sqrt{k_w * \rho_w * c_w} \tag{3.8}$$

Where, $k_w$ – thermal conductivity of workpiece

In the current investigation, effective radius of contact of abrasive grain $(r_0)$ were chosen as 20µm (Vashista, 2010)

The eqn (3.4) can be rewritten as

$$q_w - q_{ch} = \frac{q_w}{R_{ws}} + q_f \tag{3.9}$$

As per (Rowe, 2001), heat flux carried away by the grinding fluid $(q_f)$ can be expressed as

$$q_f = h_f \theta_m \tag{3.10}$$

Where, $h_f$ = convective heat transfer coefficient of grinding fluid

$\theta_m$ = maximum temperature rise in grinding zone

The value of $h_f$ were chosen as follows

$h_f$ = 0 (for dry grinding)

$h_f$ = 6700 W/$m^2.K$ (for wet grinding) (Vashista, 2010)

Maximum temperature rise in grinding zone ($\theta_m$) can be estimated using Jaeger model (Jaeger, 1942) which is based on theory of moving heat source and the same can be represented as follows

$$\theta_m = 3.543\left(\frac{2\alpha q}{\pi K v}\right)\left(\sqrt{\left(\frac{vL}{2\alpha}\right)}\right) \tag{3.11}$$

In context to grinding, $v$ = $\mathrm{V_w}$, 2L = Contact length =$L_c$, $k_w$ = thermal conductivity of workpiece material, $\alpha$ = thermal diffusivity = $\frac{k_w}{\rho * c}$ and $q$ = $q_w$ = heat flux entering the workpiece material, therefore

$$\theta_m = 3.543\left(\frac{2\alpha q_w}{\pi k_w \mathrm{V_w}}\right)\left(\sqrt{\frac{\mathrm{V_w L_c}}{4\alpha}}\right) \tag{3.12}$$

$$q_w = \frac{\theta_m \beta_w}{1.13}\left(\sqrt{\left(\frac{\mathrm{V_w}}{\mathrm{L_c}}\right)}\right) \tag{3.13}$$

Combining eqn (3.9), eqn (3.10) and eqn (3.13)

Rise in grinding temperature ($\theta_m$) is estimated as follows

$$\theta_m = \frac{q_t - q_{ch}}{h_f + \frac{\beta_w}{1.13 R_{ws}}\sqrt{\frac{\mathrm{V_w}}{L_c}}} \tag{3.14}$$

Table 3.4 represent the thermal properties of workpiece material and abrasive and is used to estimate the grinding zone temperature.

Table 3.4: Thermal properties of abrasive and workpiece material

| Melting point, $T_{mp}$(workpiece)°C | Density, $\rho_w$ (workpiece)kg/mm$^3$ | Specific heat, $c_w$ (workpiece) J/kg. °C | Thermal conductivity, $K_w$ (workpiece) W/(m.K) | Thermal conductivity, $K_g$ (grit) W/(m.K) |
|---|---|---|---|---|
| 1450 (unhardened steel)<br>1530 (hardened steel) | 7750 (unhardened steel)<br>7850 (hardened steel) | 450(unhardened steel)<br>477 (hardened steel) | 54 (unhardened steel)<br>44 (hardened steel) | 35 (alumina abrasive grit) |

## 3.5 Assessment of surface integrity:

### 3.5.1 Metallographic and microhardness analysis:

Ground samples were cut perpendicular to and along the grinding direction for microstructural analysis. These samples were thereafter hot moulded in specimen mount press (Chennai metco, India) using phenolic resin powder (Bakelite). Moulded samples were polished on different grade of emery papers with successively fine grit of mesh number 100, 200, 400, 600 and 1000 followed by cloth polishing with $Al_2O_3$ paste on auto-disc polishing machine (Chennai metco, India). The samples were then cleaned using acetone followed by etching using 2% nital solution for about 10-15 sec and after rinsed in running tap water and finally dried using hot stream of air for observation of cross section of the ground surface under an optical microscope (Dewinter). Fig.3.4 shows one such typical micrograph of ground sample.

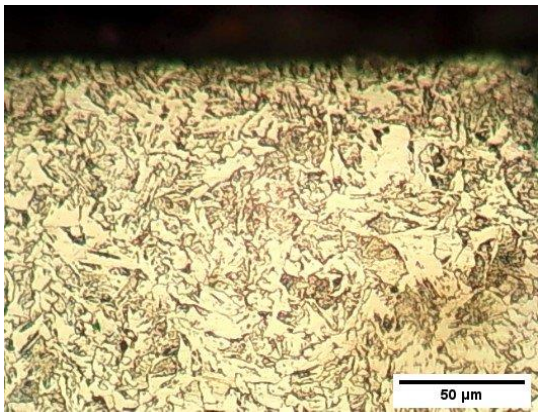


Fig.3.4 Micrograph showing the cross section of the ground sample

The microhardness (HV) testing of the ground surface were evaluated using microhardness tester (Micro Mech Technologies, India). The indentation were taken over three different locations at the same depth of 25 µm but with enough spacing to avoid overlapping of indent which were then averaged and used for analysis. This is a practical limitation because of loss of material constraint at positions closer to the surface, and a limit of 2.5 times the indentation diagonal as recommended by ASTM E92 standard.

### 3.5.2 Surface roughness analysis:

In the present study, surface roughness is discussed as per universally recognized ISO 4287:1977 Standard. The parameter, *Ra*, is used in the context which is the measure of arithmetic average of absolute vertical deviation of the roughness profile from the centre line. The surface roughness (*Ra*) was measured using Mitutoyo Surftest (SV-2100S4) with traverse length of 0.8 mm and cut-off length of 4.0 mm. To improve the accuracy of the result, readings were taken at three different positions across the grinding direction and were averaged for further analysis. Low pass Gaussian filter

were utilized in order to screen the mean line roughness profile from the original profile.

### 3.5.3 Residual stress assessment using X-ray diffraction:

X-ray diffraction (XRD) of the ground sample was performed along the grinding direction using (Rigaku Xray diffractometer) to study the nature and amount of peak shift. Scan parameters were collected with 2θ ($20^o \leq 2\theta \leq 120^o$). Gazzara (1983) in his work shows the effect of residual stress on peak position ($2\theta$), in the presence of compressive residual stress the initial position of atom gets reduced which thereby leads to an increase in ($\theta$) in accordance with Bragg's law. Similarly a decrease in ($\theta$) is observed in the presence of tensile residual stress.

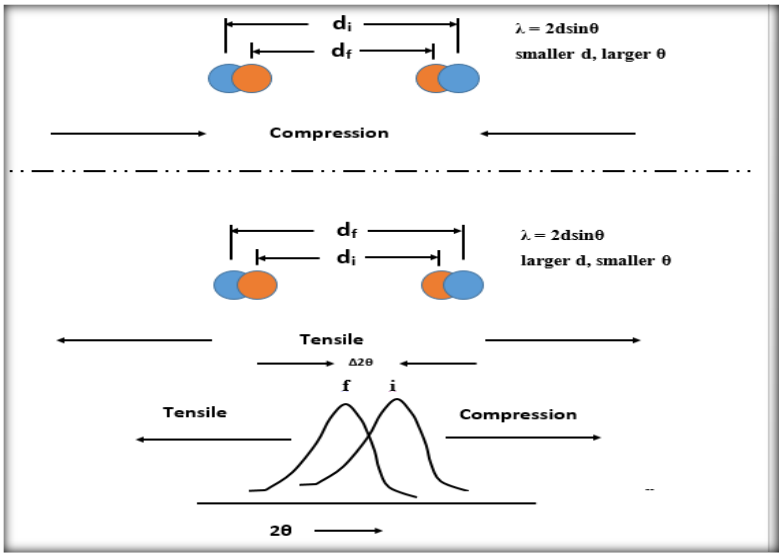


Fig.3.5 Effect of tensile and compressive residual stress on XRD peak position (Gazzara, 1983)

Fig.3.5 shows the effect of residual stress state on the shift in XRD peak position. The details of the parameter during XRD analysis is depicted in Table 3.5.

Table 3.5: Parameters for XRD analysis

| | |
|---|---|
| Radiation | Fe-Kα |
| Voltage | 40kV |
| Current | 15mA |
| Step width | 0.02 |
| Scan speed | 5 degree/min |

### 3.6 Magnetic Barkhausen noise analysis:

The magnetic Barkhausen noise signal and hysteresis loop measurements were carried out using the commercially available Magstar system supplied by Technofour, India. Measurement system as shown in Fig.3.6 consists of a flat-surface probe with U shape magnetising yoke to generate magnetic field inside the test sample with the help of current from the power supply. A pick-up coil (ferrite) at the centre was used to gather the signal generated as the magnetic response of the work material. Surface contaminants such as oil, dust etc. affects the formation of hysteresis loop. To avoid this, test samples were cleaned using acetone. The centre point of ground samples were selected for MBN and hysteresis loop measurement. To improve the accuracy of the result each observation were repeated three times and their average value is used for further analysis. The significant change in the ground samples were expected near the surface and accordingly the filtering frequency were adjusted. Table 3.6 enlist the detail of initial parameter considered for the Barkhausen noise analysis. The selection of magnetizing frequency and magnetic field intensity were based on various trial runs so

as to avoid distortion in the magnetizing signal due to magnetic coupling between the magnetizing coil and work material.

Table 3.6: Detail of initializing parameter for MBN analysis

| | |
|---|---|
| Magnetizing frequency | 100Hz |
| Magnetic field intensity | 500 Oersted |
| Gain | 20dB |
| No. of burst | 6 |
| Filter frequency | 10-300 kHz |

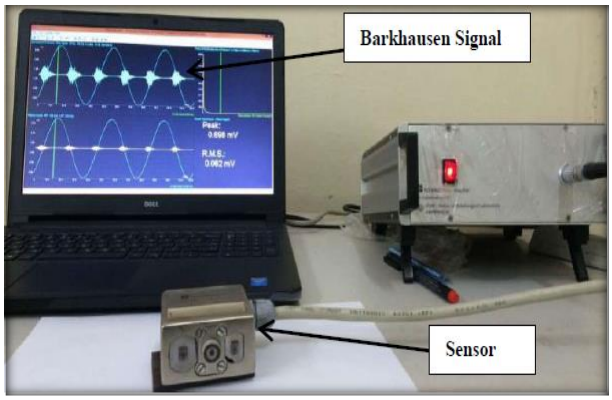


Fig.3.6 Magnetic Barkhausen noise set-up

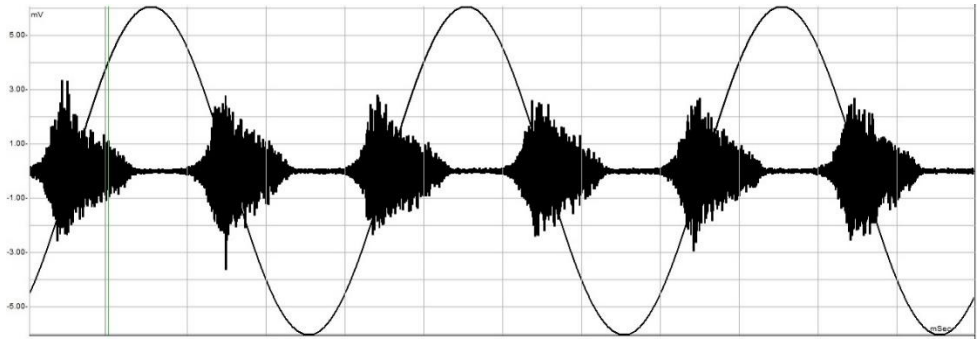

Fig.3.7 Typical Barkhausen noise burst as received from ground unhardened low carbon steel

Fig.3.7 represents the typical magnetic Barkhausen noise burst along with superimposed external magnetic excitation field as received from the ground unhardened low carbon steel. Similarly, Fig.3.8 shows the magnetic Barkhausen noise burst as received from the ground hardened low carbon steel.

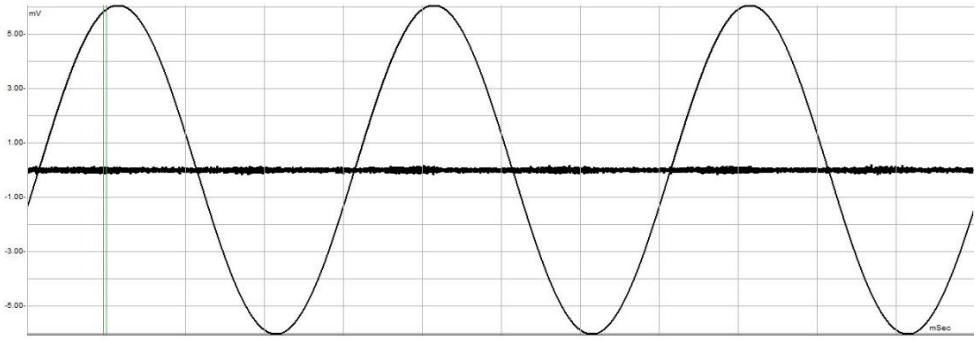


Fig.3.8 Typical Barkhausen noise burst as received from ground hardened low carbon steel

Pasley (1970) laid the foundation for stress detection using magnetic Barkhausen noise technique. It his study, he observed an increase in MBN amplitude with increasing tension and decrease in MBN amplitude with increasing compression. Moorthy *et al.*, (2005) utilizes the peak amplitude of the MBN signal to detect the change in stress during grinding of case carburized EN36 steel. Mitra and Jiles (1995) discussed the effect of stress on number of Barkhausen pulses ($N_{MBN}$). Further, Mandal *et al.*, (1997) uses Barkhausen noise energy ($MBN_{EN}$) to detect the change in stress during bending of steel. However, Wang *et al.*, (2013) shows the effect of stress on area under MBN burst ($I_{MBN}$). Langman (1987) investigated the effect of stress on the shape of hysteresis loop during plastic bending of mild steel. Stevens (2000) utilizes the parameter derived from hysteresis loop such as coercivity, saturation magnetization and remanance to detect stress level in steel under uni-axial condition.

In present investigation, root mean square value derived from magnetic Barkhausen noise signal and average permeability derived from hysteresis loop were used to analyze changes in stress upon grinding of unhardened and hardened (case- carburized) low carbon steel.

Table 3.7: Detail of initializing parameter for hysteresis loop analysis

| | |
|---|---|
| Magnetizing frequency | 1Hz |
| Magnetic field intensity | 500 Oersted |
| Waveform | sinusoidal |

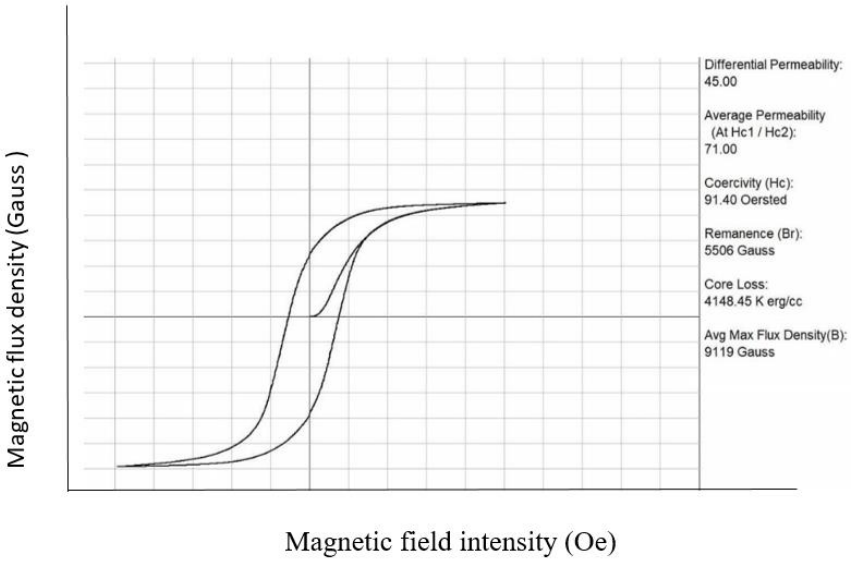


Fig.3.9 Typical hysteresis loop as received from ground steel

Fig.3.9 shows the typical hysteresis loop along with its characteristics parameter as obtained from the ground samples. Hysteresis loop represents the change in magnetization and demagnetization path of the sample when placed in external varying magnetic field. Table 3.7 enlist the detail of initial parameter considered for the hysteresis loop analysis.